Chinese Chemical Letters 36 (2025) 109919

Contents lists available at ScienceDirect

Chinese Chemical Letters

journal homepage: www.elsevier.com/locate/cclet

S-doped carbonized wood fiber decorated with sulfide heterojunction-embedded S, N-doped carbon microleaf arrays for efficient high-current-density oxygen evolution

Bin Zhao[a], Heping Luo[a], Jiaqing Liu[b], Sha Chen[a], Han Xu[a,*], Yu Liao[a], Xue Feng Lu[b,*], Yan Qing[a,*], Yiqiang Wu[a]

[a] College of Materials Science and Engineering, Central South University of Forestry and Technology, Changsha 410004, China
[b] State Key Laboratory of Photocatalysis on Energy and Environment, College of Chemistry, Fuzhou University, Fuzhou 350108, China

ARTICLE INFO

Article history:
Received 22 February 2024
Revised 22 March 2024
Accepted 23 April 2024
Available online 24 April 2024

Keywords:
Electrocatalyst
Heterojunction
Oxygen evolution reaction
Wood fiber
Sulfide

ABSTRACT

Industrial high-current-density oxygen evolution catalyst is the key to accelerating the practical application of hydrogen energy. Herein, Co_9S_8/CoS heterojunctions were rationally encapsulated in S, N-codoped carbon ((Co_9S_8/CoS)@SNC) microleaf arrays, which are rooted on S-doped carbonized wood fibers (SCWF). Benefiting from the synergistic electronic interactions on heterointerfaces and the accelerated mass transfer by array structure, the obtained self-supporting (Co_9S_8/CoS)@SNC/SCWF electrode exhibits superior performance toward alkaline oxygen evolution reaction (OER) with an ultra-low overpotential of 274 mV at 1000 mA/cm^2, a small Tafel slope of 48.84 mV/dec, and ultralong stability up to 100 h. Theoretical calculations show that interfacing Co_9S_8 with CoS can upshift the d-band center of the Co atoms and strengthen the interactions with oxygen intermediates, thereby favoring OER performance. Furthermore, the (Co_9S_8/CoS)@SNC/SCWF electrode shows outstanding rechargeability and stable cycle life in aqueous Zn-air batteries with a peak power density of 201.3 mW/cm^2, exceeding the commercial RuO_2 and Pt/C hybrid catalysts. This work presents a promising strategy for the design of high-current-density OER electrocatalysts from sustainable wood fiber resources, thus promoting their practical applications in the field of electrochemical energy storage and conversion.

© 2025 Published by Elsevier B.V. on behalf of Chinese Chemical Society and Institute of Materia Medica, Chinese Academy of Medical Sciences.

The production of hydrogen (H_2) through water electrolysis holds the potential to enable the transition from a fossil fuel economy to a low-carbon, sustainable, and affordable economy [1–3]. Currently, the development bottlenecks of water electrolysis lie in the slow kinetics of the oxygen evolution reaction (OER) and its heavy dependence on precious metals [4,5]. Industry and academia have made great progress in creating efficient and stable OER electrocatalysts, such as transition metal-based materials, including their alloys, oxides/hydroxides, and other related compounds, as well as their composites [6–9]. Unfortunately, most OER electrocatalysts only perform well at low current densities (<100 mA/cm^2) over a limited lifetime [10] and thus fail to meet the expectations of the European Fuel Cell and Hydrogen Consortium for industrial alkaline electrolysis, *i.e.*, current density higher than 800 mA/cm^2 at an overpotential less than 300 mV with good long-term stability (≥100 h) [11–13]. Therefore, an electrocatalyst that can efficiently and stably catalyze OER at industrial-grade high current densities is the key to accelerating the practical application of hydrogen energy.

At high current densities, the OER performance is limited by mass transfer obstruction caused by large amounts of oxygen products [14–16]. The nanoarray, featuring an open frame, facilitates the enhanced penetration of electrolytes and the efficient diffusion of O_2 bubbles, thereby ensuring the rapid mass transfer process during OER at high current density [17–19]. In addition to speeding up the mass transfer process, reducing the overpotential of the OER at high current densities can be achieved by decoupling the scaling relationships of the reaction intermediates [20–22]. The construction of heterojunction materials can break the scaling relationship of OER intermediates due to its abundant interface sites, spatial distribution of intermediates, unique electronic structures, and novel synergistic effects [23,24]. However, the synthesis of heterojunction materials typically requires multiple steps and accurate molar ratios of each component, which increases the cost of heterojunction materials preparation. In addition, the stable potential

* Corresponding authors.
E-mail addresses: xuh@csuft.edu.cn (H. Xu), luxf@fzu.edu.cn (X.F. Lu), qingyan@csuft.edu.cn (Y. Qing).

https://doi.org/10.1016/j.cclet.2024.109919
1001-8417/© 2025 Published by Elsevier B.V. on behalf of Chinese Chemical Society and Institute of Materia Medica, Chinese Academy of Medical Sciences.

intervals of different components may conflict, leading to interface instability and thus affecting the catalytic stability of the heterojunction materials [25–27]. Zeolitic imidazolate frameworks (ZIFs) are porous materials with tunable composition, which are the ideal precursors for heterojunction nanoarray materials and have great potential in electrocatalytic applications [28,29]. In recent years, researchers have attempted to incorporate carbon materials such as carbon fibers and graphene into ZIFs as substrates for the preparation of supported electrocatalysts, aiming to mitigate the issue of active site reduction caused by agglomeration [30–32]. However, precisely tuning the interface between ZIF and substrate *via* a simple preparation method remains challenging. Moreover, most of the aforementioned substrates are derived from petrochemical sources, thereby lacking ecological sustainability [33]. In addition, at high current densities, the active species will inevitably be shed from the substrate, leading to a significant discount of stability. Therefore, the introduction of more eco-friendly, efficient, and stable substrates is of great strategic importance in the preparation of ZIFs-derived supported electrocatalysts.

Compared with common carbon substrates, wood fiber (WF), being an abundant and eco-friendly biomass material, possesses rich hydroxyl groups on its surface, thereby providing an inherent platform for the integration of exogenous heterogeneous functional components without complicated operations [34,35]. Therefore, WF has a high research potential and exploration value as a substitute for traditional petrochemical carbon materials. Herein, a ZIFs-derived microleaf array supported electrocatalyst was prepared by a simple synchronous carbonization and sulfidation process. The microleaf arrays were directly anchored on S-doped carbonized wood fibers (SCWF), where the microleaf arrays were composed of an S and N co-doped carbon (SNC) matrix encapsulating abundant Co_9S_8/CoS heterojunction nanoparticles. Thanks to the unique structural effect of the supported catalyst, the obtained (Co_9S_8/CoS)@SNC/SCWF effectively mitigates the agglomeration issues commonly encountered in carbon composites derived from ZIFs, thereby enabling a significantly enhanced specific surface area and electrical conductivity. At the same time, the strongly coupled nanointerfaces efficiently adjust the electronic structure and benefit the electron transfer of the heterostructure, thereby optimizing the adsorption and desorption of reaction intermediates, giving excellent OER performance. Encouragingly, (Co_9S_8/CoS)@SNC/SCWF requires only a low overpotential of 274 mV to achieve an industrial-grade high current density of 1000 mA/cm^2 for OER. In addition, the average decay rate was only 38 μV/h at 1000 mA/cm^2. Density functional theory (DFT) calculations validate the interfacial effect of Co_9S_8 coupling with CoS, which leads to an upward shift in the d-band center of Co atoms and charge redistribution across the heterojunction interface, thereby disrupting the scaling relationship of the intermediate. In the application of zinc-air battery (ZAB), the (Co_9S_8/CoS)@SNC/SCWF shows outstanding rechargeability and stable cycle life with a peak power density of 201.3 mW/cm^2, exceeding the commercial RuO_2 and Pt/C hybrid catalysts.

The synthesis diagram of (Co_9S_8/CoS)@SNC/SCWF is shown in Fig. 1. Firstly, WF is added to a solution containing cobalt nitrate at room temperature, the abundant hydroxyl groups on the surface of WF allow Co^{2+} ions to be fully adsorbed on its surface. The Fourier transform infrared spectroscopy (FTIR) spectra show that the vibration intensity at the tensile vibration peak significantly reduces after metal ion adsorption, indicating the successful adsorption of metal ions (Fig. S1 in Supporting information) [36]. The peaks observed at $2\theta = 14.2°$ and 22.5° in the X-ray diffraction (XRD) patterns of natural WF correspond to the crystallographic planes of (101) and (002), respectively, in the structure of cellulosic cellulose (Fig. S2a in Supporting information) [37]. Co^{2+} was pre-adsorbed onto the natural WF surface with a diameter of 20–

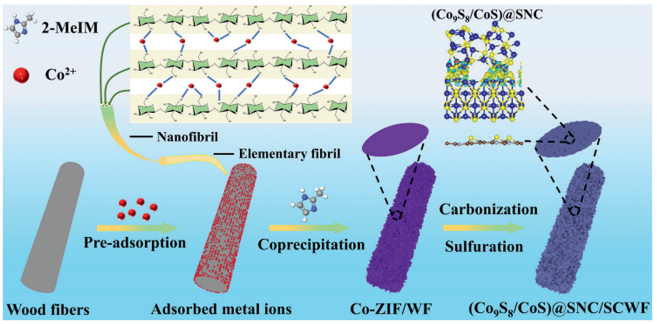

Fig. 1. Schematic illustration of the synthetic process of (Co_9S_8/CoS)@SNC/SCWF.

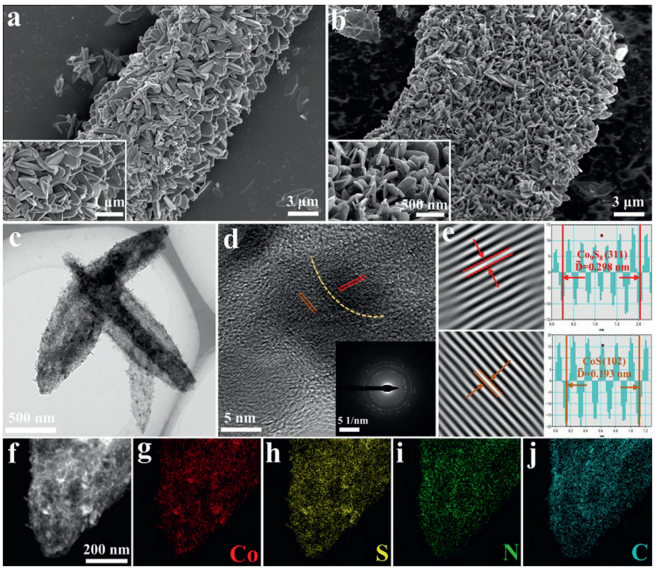

Fig. 2. SEM images of (a) Co-ZIF/WF and (b) (Co_9S_8/CoS)@SNC/SCWF with different magnifications. (c) TEM image of (Co_9S_8/CoS)@SNC. (d) HRTEM image of (Co_9S_8/CoS)@SNC (the inset is the corresponding SAED pattern). (e) The IFFT image of (Co_9S_8/CoS)@SNC/SCWF and corresponding lattice spacing. (f-j) HAADF-STEM image and corresponding elemental mappings of (Co_9S_8/CoS)@SNC.

30 μm (Fig. S2b in Supporting information), facilitating the subsequent uniform anchoring of microleaf-like ZIF particles grown on the surface (Fig. S3 in Supporting information), denoted as Co-ZIF/WF. The Co-ZIF/WF precursor was annealed under an N_2 atmosphere, and the composite electrocatalyst (Co_9S_8/CoS)@SNC/SCWF was obtained through a simultaneous carbonization and sulfidation process. When the Co-ZIF/WF precursor was thermally decomposed at 700 °C in an N_2 atmosphere in the presence of sublimed sulfur, the coordinated Co^{2+} within Co-ZIF was effectively reduced to metallic cobalt. Subsequently, this metallic Co reacted with sulfur vapor to form a Co_9S_8/CoS heterojunction. Simultaneously, the 2-MeIM linker and WF were concurrently transformed into SNC and SCWF, respectively. The structural characterization of SCWF by XRD and scanning electron microscopy (SEM) was performed (Fig. S4 in Supporting information).

SEM images were employed to analyze the morphology of Co-ZIF/WF and (Co_9S_8/CoS)@SNC/SCWF. In Fig. 2a, the uniform microleaf arrays were observed on the WF substrate. After simultaneous carbonization and sulfidation, the surface roughness of the microleaf arrays is enhanced while maintaining their structural integrity (Fig. 2b), which increases the surface area of (Co_9S_8/CoS)@SNC/SCWF to provide more active sites for the reaction, and the space between the microleaf arrays is conducive to the full diffusion of the electrolyte. SEM images of Co-ZIF, Co@NC/CWF, and (Co_9S_8/CoS)@SNC are

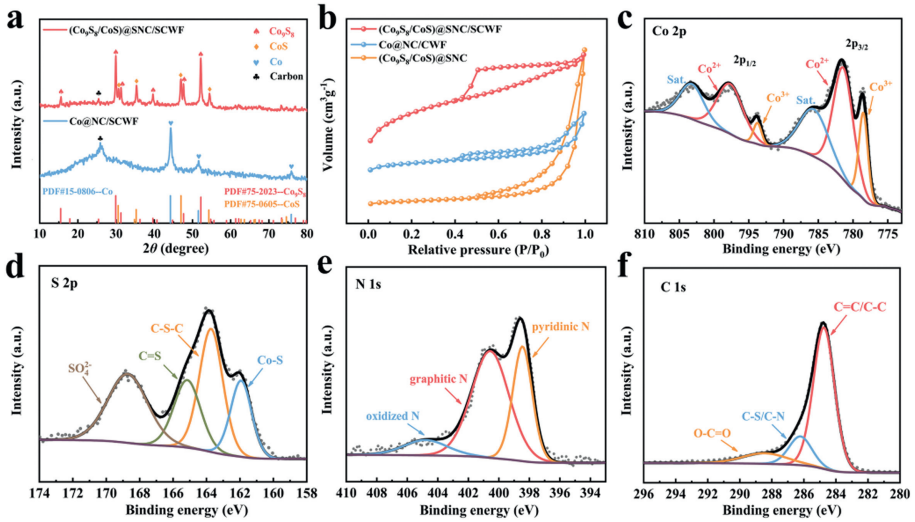

Fig. 3. (a) XRD patterns of (Co_9S_8/CoS)@SNC/SCWF and Co@NC/CWF. (b) N_2 adsorption-desorption isothermal curves for (Co_9S_8/CoS)@SNC/SCWF, Co@NC/CWF and (Co_9S_8/CoS)@SNC. The high-resolution XPS spectrum of (c) Co 2p, (d) S 2p, (e) N 1s and (f) C 1s for (Co_9S_8/CoS)@SNC/SCWF.

provided in Fig. S5 (Supporting information). Moreover, TEM image of (Co_9S_8/CoS)@SNC/SCWF indicates the detailed structure of the microleaf arrays (Fig. 2c). The high-resolution TEM (HRTEM) and inverse fast Fourier transform (IFFT) images of (Co_9S_8/CoS)@SNC/SCWF (Figs. 2d and e) reveal two distinct lattice fringes with interplanar spacings of 0.298 nm and 0.193 nm, respectively, corresponding to the (311) plane of Co_9S_8 and the (102) plane of CoS. Selected-area electron diffraction (SAED) pattern clearly shows both spot and ring features, providing unequivocal evidence for the polycrystalline nature of the (Co_9S_8/CoS)@SNC heterojunction. High-angle annular dark-field scanning transmission electron microscopy (HAADF-STEM) and corresponding elemental mapping images (Figs. 2f–j) demonstrate that Co, S, N, and C are uniformly distributed throughout the microleaf arrays.

The crystalline structure of the electrocatalyst was thoroughly examined using XRD (Fig. 3a). In the XRD pattern of (Co_9S_8/CoS)@SNC/SCWF, the diffraction peaks located at 15.5°, 29.9°, 31.3°, 39.6°, 47.7°, and 52.2° can be indexed to the (111), (311), (222), (331), (511), and (440) planes of Co_9S_8, respectively (PDF#75-2023). Additionally, the peaks at 30.5°, 35.3°, 46.9°, and 54.3° can be ascribed to the (100), (101), (102), and (110) planes of CoS, respectively (PDF#75-0605). Coupled with the results from TEM, it has been conclusively demonstrated that a Co_9S_8/CoS heterostructure was successfully synthesized in (Co_9S_8/CoS)@SNC/SCWF through a simple synchronous carbonization and sulfidation process. In the XRD pattern of Co@NC/CWF, distinct diffraction peaks at 44.2°, 51.5°, and 75.9° can be discerned, which are correspondingly indexed to the (111), (200), and (220) planes of face-centered cubic metallic Co (PDF#15-0806). At the carbon peak near 25°, Co@NC/CWF presents a more pronounced sharpness than (Co_9S_8/CoS)@SNC/SCWF, suggesting superior crystallinity in the Co@NC/CWF catalyst. The diminished crystallinity in (Co_9S_8/CoS)@SNC/SCWF might be attributed to the introduction of S, leading to a higher density of defects. Raman spectroscopy was employed to further elucidate the impact of S doping on (Co_9S_8/CoS)@SNC/SCWF. The Raman spectra of (Co_9S_8/CoS)@SNC/SCWF and Co@NC/CWF (Fig. S6 in Supporting information), manifest two distinct characteristic peaks at 1334 cm^{-1} and 1585 cm^{-1}. Correlating with the D and G bands of carbon, the intensity ratio of D to G bands for (Co_9S_8/CoS)@SNC/SCWF is 1.03, surpassing the Co@NC/CWF, (Co_9S_8/CoS)@SNC and SCWF. This suggests that S doping and the structural effects of the supported electrocatalyst has promoted the formation of a highly disordered phase and a plethora of defects within the amorphous carbon layer, resonating with the findings from XRD analysis [38]. The XRD pattern of (Co_9S_8/CoS)@SNC (Fig. S7 in Supporting information) distinctly presents two sets of peaks, which are respectively attributed to the Co_9S_8 and CoS phases. N_2 adsorption-desorption experiments were employed to investigate the specific surface area and pore size distribution of the electrocatalysts (Fig. 3b). Brunauer-Emmett-Teller (BET) analysis shows that the surface area and pore volume of (Co_9S_8/CoS)@SNC/SCWF is 252.05 m^2/g and 0.16 cm^3/g, respectively. These values exceed those of Co@NC/CWF (128.92 m^2/g and 0.11 cm^3/g) and (Co_9S_8/CoS)@SNC (23.01 m^2/g and 0.07 cm^3/g). The relative aperture distribution (Fig. S8 in Supporting information) indicates (Co_9S_8/CoS)@SNC/SCWF has the most mesopores, which can provide more active sites and reaction areas.

The composition and valence states of (Co_9S_8/CoS)@SNC/SCWF were meticulously investigated using X-ray photoelectron spectroscopy (XPS). The acquired XPS spectrum for (Co_9S_8/CoS)@SNC/SCWF shows the presence of Co, S, N, and C elements (Fig. S9 in Supporting information). The existential O may be attributed to the surface oxidation of the (Co_9S_8/CoS)@SNC/SCWF. The high-resolution Co 2p XPS spectrum of (Co_9S_8/CoS)@SNC/SCWF (Fig. 3c) manifests four predominant peaks: Co $2p_{1/2}$ at 797.6 and 793.7 eV, and Co $2p_{3/2}$ at 781.3 and 778.5 eV. The peaks positioned at 781.3 and 797.6 eV denote the existence of Co^{2+}, while those at 778.5 and 793.7 eV indicate the presence of Co^{3+} [39,40]. Given the various sulfur species in (Co_9S_8/CoS)@SNC/SCWF, the high-resolution S 2p XPS spectrum (Fig. 3d) reveals multiple peaks. The peak at 161.9 eV is ascribed to Co−S bonds. The peak at around 163.8 eV can be ascribed to C−S−C bonds, while the peak at 165.2 eV corresponds to the C=S bonds. The peak situated at 168.7 eV is associated with sulfate components, suggesting potential surface oxidation of the sulfide materials in ambient air [41–43]. The high-resolution XPS spectrum of N 1s (Fig. 3e) shows that the doped N is mainly in the form of pyridine N, graphite N, and oxidized N [44–46]. The high-resolution C 1s XPS spectrum (Fig. 3f) reveals characteristic peaks at 284.8, 286.2, and 288.4 eV, which are correspondingly ascribed to C=C/C-C, C–S/C–N, and O–C=O bonds. This confirms the successful synthesis of a carbon matrix co-doped with S and N. To ascertain the successful doping of S into both (Co_9S_8/CoS)@SNC and SCWF, XPS spectrum for (Co_9S_8/CoS)@SNC and SCWF were gathered (Fig. S10 in Supporting information).

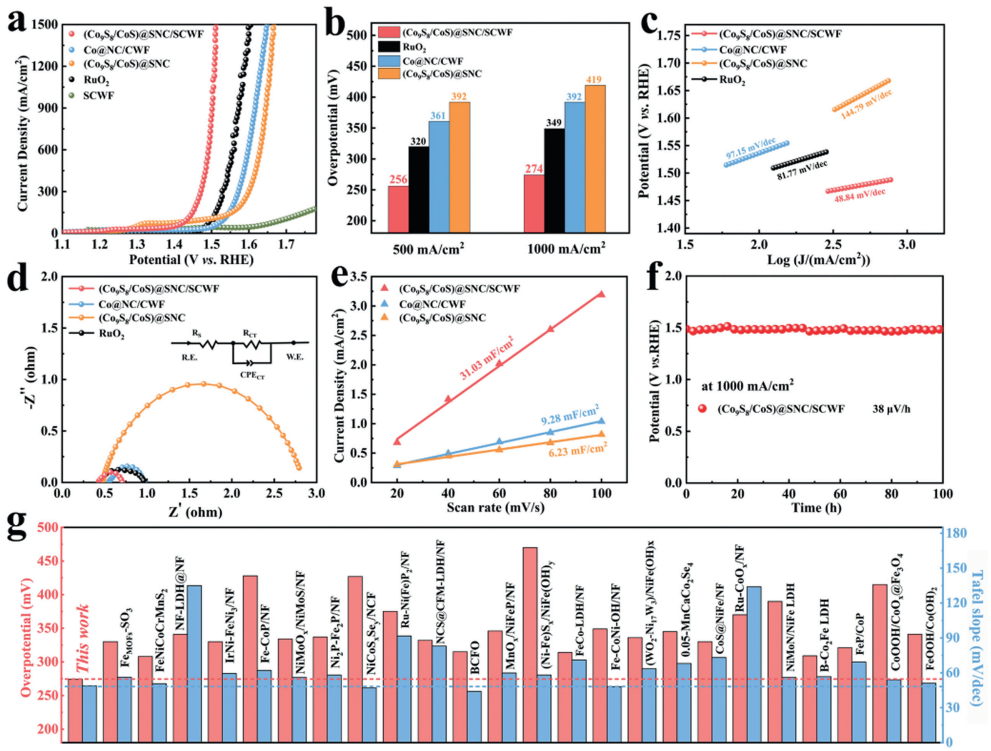

Fig. 4. (a) LSV curves of (Co_9S_8/CoS)@SNC/SCWF, Co@NC/CWF, (Co_9S_8/CoS)@SNC, commercial RuO_2, and SCWF. (b) Overpotentials at 500 and 1000 mA/cm^2. (c) The corresponding Tafel slopes. (d) Nyquist plots of (Co_9S_8/CoS)@SNC/SCWF, Co@NC/CWF (Co_9S_8/CoS)@SNC, and commercial RuO_2 in 6.0 mol/L KOH (Insert is the corresponding equivalent circuit). (e) Current density as a function of scan rate for (Co_9S_8/CoS)@SNC/SCWF, Co@NC/CWF, and (Co_9S_8/CoS)@SNC. (f) The chronopotentiometry response of (Co_9S_8/CoS)@SNC/SCWF at 1000 mA/cm^2 for OER. (g) Comparisons of overpotential at 1000 mA/cm^2 and Tafel slope with literature (reference samples are presented in Table S2).

For both (Co_9S_8/CoS)@SNC and SCWF, the high-resolution S 2p XPS spectrum distinctly identifies the C=S bonds. Additionally, the characteristic peak of the C–S bonds is discernible in the C 1s spectrum. These observations unequivocally confirm the doping of S into (Co_9S_8/CoS)@SNC and SCWF. The high-resolution Co 2p XPS spectrum of (Co_9S_8/CoS)@SNC/SCWF, Co@NC/CWF, and (Co_9S_8/CoS)@SNC were meticulously compared (Fig. S11 in Supporting information). Notably, there is a discernible positive shift in the binding energy of Co 2p in (Co_9S_8/CoS)@SNC/SCWF compared to that of Co@NC/CWF and (Co_9S_8/CoS)@SNC. The incorporation of S doping into the carbon matrix and the introduction of SCWF can effectively modulate the electronic structure, resulting in distinctive surface reactivity that enhances the OER performance of (Co_9S_8/CoS)@SNC/SCWF [47,48].

To evaluate the practical application, we compared the OER performance of (Co_9S_8/CoS)@SNC/SCWF, Co@NC/CWF, (Co_9S_8/CoS)@SNC, SCWF, and commercial RuO_2 with the same loadings in a typical three-electrode setup with 6.0 mol/L KOH electrolyte solution. Obviously, (Co_9S_8/CoS)@SNC/SCWF sample exhibited better OER catalytic activity (Figs. 4a and b), requiring only low overpotential of 256 and 274 mV to drive current densities of 500 and 1000 mA/cm^2, respectively. It was superior to commercial RuO_2 (320 mV at j_{500}, 349 mV at j_{1000}), Co@NC/CWF (361 mV at j_{500}, and 392 mV at j_{1000}) and (Co_9S_8/CoS)@SNC (392 mV at j_{500}, 419 mV at j_{1000}), and the SCWF had almost no electrochemical activity for OER at high current densities. Meanwhile, the Tafel slope of (Co_9S_8/CoS)@SNC/SCWF (48.84 mV/dec) is also lower than that of RuO_2 (81.77 mV/dec), Co@NC/CWF (97.15 mV/dec) and (Co_9S_8/CoS)@SNC (144.79 mV/dec), which demonstrates that (Co_9S_8/CoS)@SNC/SCWF have the faster OER reaction kinetics (Fig. 4c). The electrochemical impedance spectroscopy (EIS) shows that (Co_9S_8/CoS)@SNC/SCWF has a charge transfer resistance of 0.26 Ω (Fig. 4d), further confirming its excellent OER charge transfer kinetics, which is consistent with the results of low overpotential and small Tafel slope. The equivalent circuit diagram is shown in Fig. 4d, and the corresponding fitting data is shown in (Table S1 in Supporting information).

To further investigate the intrinsic catalytic activity of the different samples, the electrochemical surface area (ECSA) was investigated. ECSA is an important criterion for quantifying the number of exposed active sites, which is proportional to the electrochemical bilayer capacitance (C_{dl}) [49]. Typically, the cyclic voltammetry (CV) method is employed within the non-Faraday potential range to determine the C_{dl} of the sample by employing various sweep rates. As shown in Fig. 4e and Fig. S12 (Supporting information), the C_{dl} value of (Co_9S_8/CoS)@SNC/SCWF (31.03 mF/cm^2) is significantly higher compared to that of Co@NC/CWF (9.28 mF/cm^2) and (Co_9S_8/CoS)@SNC (6.23 mF/cm^2). The higher C_{dl} values of (Co_9S_8/CoS)@SNC/SCWF may be attributed to the porous heterojunction structure as well as the uniform anchoring of microleaf arrays on SCWF, which expose a large number of reactive active sites for OER. To more reliably assess the intrinsic catalytic activity, we obtained the ECSA-normalized LSV curves (Fig. S13 in Supporting information). Significantly, (Co_9S_8/CoS)@SNC/SCWF exhibits an impressive intrinsic catalytic activity, as evidenced by its ability to achieve a normalized current density of 1 mA/cm^2 with a minimal overpotential of only 268 mV. The turnover frequency value of (Co_9S_8/CoS)@SNC/SCWF is 223.61 s^{-1} at an overpotential of 274 mV (Fig. S14 in Supporting information), much higher than those of (Co_9S_8/CoS)@SNC (23.31 s^{-1}) and Co@NC/CWF (10.95 s^{-1}). Based on the generated oxygen volume, we measured the Faraday efficiency of Co_9S_8/CoS)@SNC/SCWF at 1.47 V *vs.* RHE to be 95% (Fig. S15 in Supporting information).

The stability of the electrocatalyst in the practical application should be considered an important indicator. The chronopotentiometry response of 1000 mA/cm^2 in 6.0 mol/L KOH solution for

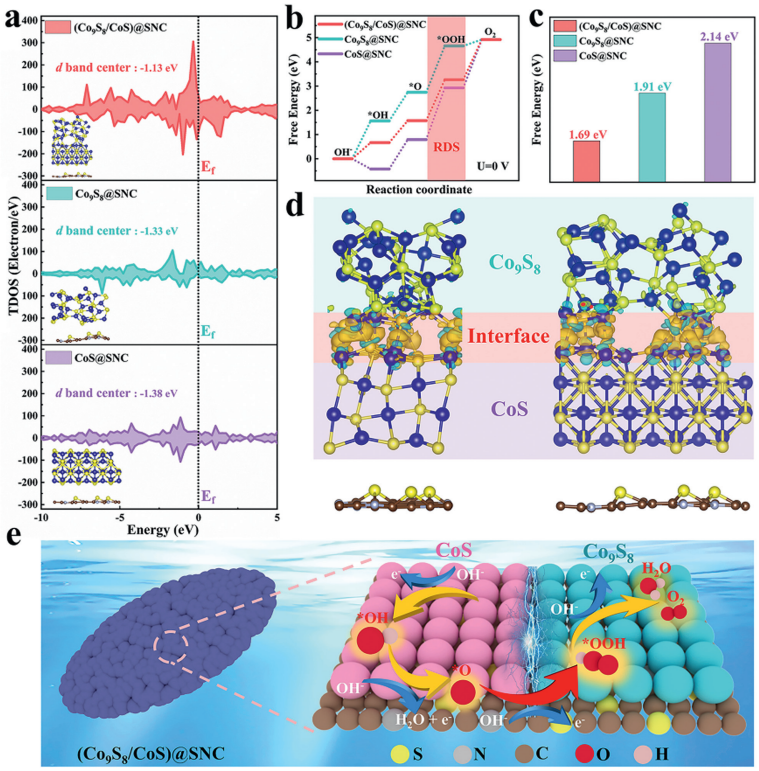

Fig. 5. (a) DOS of (Co_9S_8/CoS)@SNC, Co_9S_8@SNC, and CoS@SNC. (b) OER free energy ladder diagram of (Co_9S_8/CoS)@SNC, Co_9S_8@SNC, and CoS@SNC at *U* of 0 V. (c) RDS energy barrier comparison of different structural configurations at *U* of 0 V. (d) Charge density difference of (Co_9S_8/CoS)@SNC under different viewing angles (yellow and blue colors denote the accumulation and depletion of electrons). (e) Mechanism analysis.

(Co_9S_8/CoS)@SNC/SCWF is shown in Fig. 4f. After a stability test lasting 100 h, the potential growth of (Co_9S_8/CoS)@SNC/SCWF was found to be almost negligible (38 μV/h), demonstrating exceptional stability even at high current densities. The LSV curves (Fig. S16 in Supporting information) demonstrates almost no activity loss before and after stability test of 100 h. In addition, the XRD patterns and SEM images of (Co_9S_8/CoS)@SNC/SCWF after stability testing (Fig. S17 in Supporting information) indicate that the composition and microleaf array morphology do not change much, demonstrating its potential for industrial applications. Impressively, the OER performance of (Co_9S_8/CoS)@SNC/SCWF is better in 6.0 mol/L KOH than that in 1.0 mol/L KOH (Fig. S18 in Supporting information) and superior to that of recently reported state-of-the-art electrocatalysts at high current densities (Fig. 4g and Table S2 in Supporting information). The high-resolution XPS spectrum of Co 2p of (Co_9S_8/CoS)@SNC/SCWF after stability testing (Fig. S19a in Supporting information) shows a clear increase in the proportion of trivalent cation after OER, which is consistent with hydroxide formation. The high-resolution XPS spectrum of S 2p shows (Fig. S19b in Supporting information) that the peak intensity is significantly reduced compared to that before OER, indicating the conversion of sulfide to (oxy)hydroxide. In the high-resolution XPS spectrum of O 1s (Fig. S19c in Supporting information), the peak of M−O bonds was significantly enhanced after OER, and a new peak at 531.1 eV was observed, which was attributed to the reconstructed hydroxide (OH^-). The above results provide evidence for the formation of (oxy)hydroxides through self-remodeling following OER, as observed in Co_9S_8/CoS@SNC/SCWF [50,51].

To reveal the synergistic electronic interactions on heterointerfaces and the promotion on OER performance, density functional theory (DFT) calculations were conducted. Structural models of (Co_9S_8/CoS)@SNC, Co_9S_8@SNC, and CoS@SNC were constructed (Fig. S20 in Supporting information). The density of states (DOS) show that (Co_9S_8/CoS)@SNC, Co_9S_8@SNC, and CoS@SNC are all continuous around the Fermi level (Fig. 5a), suggesting that they all have metallic properties [52]. Higher conductivity has been observed in higher energy levels near the Fermi level, and the DOS strength at the Fermi level for the (Co_9S_8/CoS)@SNC heterojunction is significantly greater than that of the single-component heterojunction system. These results indicate that the coupling of Co_9S_8 and CoS can promote the electron transfer and thus facilitates the OER process [53]. It is also found that the d-band center of (Co_9S_8/CoS)@SNC is −1.13 eV, which is higher than that of Co_9S_8@SNC (−1.33 eV) and CoS@SNC (−1.38 eV), indicating the interactions between adsorbate and catalyst surface is strengthened after the formation of (Co_9S_8/CoS)@SNC heterointerfaces [54]. To further investigate the catalytic mechanism of (Co_9S_8/CoS)@SNC for OER, we calculated the Gibbs free energies of the intermediates for each of the basic steps of (Co_9S_8/CoS)@SNC (Fig. S21 in Supporting information), Co_9S_8@SNC (Fig. S22 in Supporting information), and CoS@SNC (Fig. S23 in Supporting information), respectively. The free energy diagram for the OER in Fig. 5b shows that the rate-determining step (RDS) of (Co_9S_8/CoS)@SNC, Co_9S_8@SNC, and CoS@SNC is the generation of *OOH intermediates (ΔG_3). The RDS energy barrier of (Co_9S_8/CoS)@SNC is 1.69 eV, which is smaller than 1.91 eV of Co_9S_8@SNC and 2.14 eV of CoS@SNC (Fig. 5c). The differential charge maps from Fig. 5d reveal that electron transfer is significantly enhanced at the interfaces between Co_9S_8 and CoS, as indicated by the accumulation (yellow) and depletion (blue) of electrons. Moreover, the redistribution of charges across this interface effectively weakens the oxygen bond on the catalyst surface while preventing excessive bonding between *O and *OOH, thereby facilitating the decoupling of the scaling relationship among intermediates [55,56]. Simultaneously, the coupling of Co_9S_8 and CoS induces an upward shift of the d-band center of Co atoms, leading to charge redistribution across the interfaces. This effect lowers

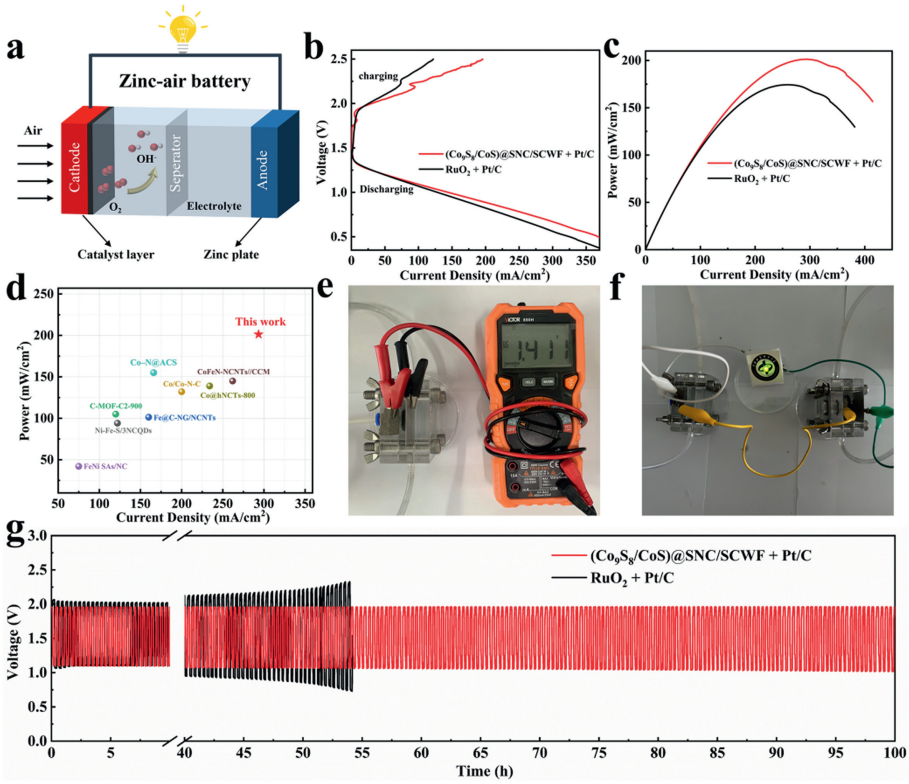

Fig. 6. (a) Schematic diagram of ZAB. (b) Charge-discharge curves of ZAB loaded with (Co_9S_8/CoS)@SNC/SCWF + Pt/C and RuO_2 + Pt/C. (c) Power density curves. (d) Comparison with recently reported ZAB performance. (e) Open circuit voltage of ZAB loaded by (Co_9S_8/CoS)@SNC/SCWF + Pt/C and (f) the photograph of a LED bulb powered by two home-made ZABs in series with (Co_9S_8/CoS)@SNC/SCWF + Pt/C as the air cathode. (g) Long-term cycling performance at 10 mA/cm^2 with (Co_9S_8/CoS)@SNC/SCWF + Pt/C and RuO_2 + Pt/C as the air cathode.

the RDS energy barrier and enhances catalytic performance (Fig. 5e). In summary, the formation of heterostructure accelerates the charge transfer at the interfaces and lowers the RDS energy barrier, thereby synergistically promoting the improvement of electrocatalytic performance.

Zinc-air battery (ZAB) possesses the advantages of secure, environmentally friendly, thereby garnering escalating attention from researchers [57,58]. We fabricated a rechargeable ZAB employing (Co_9S_8/CoS)@SNC/SCWF + Pt/C as the cathode and zinc plate as the anode to investigate its potential in practical application devices (Fig. 6a). As shown in Fig. 6b, thanks to the superior OER activity of (Co_9S_8/CoS)@SNC/SCWF than RuO_2, (Co_9S_8/CoS)@SNC/SCWF + Pt/C exhibits a smaller voltage gap during the charge and discharge process. A sudden drop at about 100 mA/cm^2 during charging is due to the generated oxygen bubbles, which is also observed in other published work [59,60]. In Fig. 6c, the max power density of (Co_9S_8/CoS)@SNC/SCWF + Pt/C (201.3 mW/cm^2) is higher than that of RuO_2 + Pt/C (174.3 mW/cm^2), which is better than most ZABs performance reported at the same time (Fig. 6d and Table S3 in Supporting information). Fig. 6e shows that the open circuit voltage of a ZAB loaded with (Co_9S_8/CoS)@SNC/SCWF + Pt/C is 1.41 V, which can successfully light up the light-emitting diode (Fig. 6f). Fig. 6g also reveals superior cycle stability of (Co_9S_8/CoS)@SNC/SCWF + Pt/C, superior to that of RuO_2 + Pt/C. These above results confirm the excellent performance of (Co_9S_8/CoS)@SNC/SCWF in ZAB.

In summary, we successfully encapsulated Co_9S_8/CoS heterojunction nanoparticles in an S and N co-doped carbon matrix and anchored them uniformly on the SCWF substrate to form microleaf arrays by a synchronous carbonization and sulfidation strategy. The heterojunction interface effect in (Co_9S_8/CoS)@SNC can facilitate the scaling relationship of the intermediate and greatly improve the catalytic performance for OER. Due to the unique structural effect of microleaf arrays, the (Co_9S_8/CoS)@SNC/SCWF electrocatalyst prevents active particle agglomeration and provides a large specific surface area for the reaction. (Co_9S_8/CoS)@SNC/SCWF shows excellent performance in the high-current-density oxygen evolution. Only a low overpotential of 274 mV is needed to achieve an industrial-grade high-current density of 1000 mA/cm^2, and the Tafel slope is as low as 48.84 mV/dec. Impressively, (Co_9S_8/CoS)@SNC/SCWF exhibited extremely excellent stability at an industrial-grade high current density of 1000 mA/cm^2, with almost no attenuation of catalytic activity (only 38 μV/h) after 100 h. As a cathode catalyst for ZAB, its power density is up to 201.3 mW/cm^2, which has broad application prospects. DFT analysis reveals that the heterojunction interface effect in (Co_9S_8/CoS)@SNC can induce the center of the d-band of Co atoms to shift up and redistribute the charge across the interface, thereby boosting the scaling relationship of the intermediate and reducing the RDS energy barrier of OER. This work presents a design approach for efficient high-current-density OER electrocatalysts using sustainable wood fiber resources.

Declaration of competing interest

The authors declare that they have no known competing financial interests or personal relationships that could have appeared to influence the work reported in this paper.

CRediT authorship contribution statement

Bin Zhao: Data curation, Formal analysis, Writing – original draft. **Heping Luo:** Validation, Visualization. **Jiaqing Liu:** Validation, Visualization. **Sha Chen:** Validation, Visualization, Writing –

review & editing. **Han Xu:** Conceptualization, Supervision, Validation, Visualization, Writing – review & editing. **Yu Liao:** Validation, Visualization. **Xue Feng Lu:** Conceptualization, Supervision, Validation, Writing – review & editing. **Yan Qing:** Supervision, Validation, Visualization, Writing – review & editing. **Yiqiang Wu:** Writing – review & editing.

Acknowledgments

This work was supported by National Key Research and Development Program of China (No. 2023YFD2200503), the Young Elite Scientists Sponsorship Program from National Forestry and Grassland Administration of China (No. 2019132614), the Science and Technology Innovation Program of Hunan Province (Nos. 2021RC3103 and 2022RC3054), and the Scientific Research Project of Hunan Provincial Education Department (Nos. 23B0276 and 21B0225). The authors also thank Shiyanjia Lab (www.shiyanjia.com) for the support of TEM and XPS tests.

Supplementary materials

Supplementary material associated with this article can be found, in the online version, at doi:10.1016/j.cclet.2024.109919.

References

[1] M.S. Dresselhaus, I.L. Thomas, Nature 414 (2001) 332–337.
[2] X.F. Lu, L. Yu, X.W. Lou, Sci. Adv. 5 (2019) eaav6009.
[3] C.F. Li, L.J. Xie, J.W. Zhao, et al., Appl. Catal. B: Environ. 306 (2022) 121097.
[4] Y. Zhang, G. Zhang, M. Zhang, et al., Chem. Eng. J. 433 (2022) 133577.
[5] K. Jiang, M. Luo, M. Peng, et al., Nat. Commun. 11 (2020) 2701.
[6] L. Li, P. Wang, Q. Shao, X. Huang, Adv. Mater. 33 (2021) 2004243.
[7] H. Wang, S. Zhu, J. Deng, et al., Chin. Chem. Lett. 32 (2021) 291–298.
[8] X.F. Zhang, W.H. Huang, L. Yu, et al., Carbon Energy 6 (2024) e362.
[9] W.H. Huang, T.T. Bo, S.W. Zuo, et al., SusMat 2 (2022) 466–475.
[10] Z. Li, X. Zhang, Z. Zhang, et al., Appl. Catal. B: Environ. 325 (2023) 122311.
[11] Y. Luo, Z. Zhang, M. Chhowalla, B. Liu, Adv. Mater. 34 (2022) 2108133.
[12] X. Xie, L. Du, L. Yan, et al., Adv. Funct. Mater. 32 (2022) 2110036.
[13] J. Chen, J. Chen, H. Cui, C. Wang, ACS Appl. Mater. Interfaces 11 (2019) 34819–34826.
[14] S. Niu, W.J. Jiang, T. Tang, et al., Adv. Sci. 4 (2017) 1700084.
[15] X. Wu, H.B. Zhang, S.W. Zuo, et al., Nano Micro Lett. 13 (2021) 136.
[16] S.L. Yu, C.X. Guo, J.N. Wang, et al., Nat. Commun. 13 (2022) 6171.
[17] X. Yu, Z.Y. Yu, X.L. Zhang, et al., J. Am. Chem. Soc. 141 (2019) 7537–7543.
[18] T. Kou, S. Wang, R. Shi, et al., Adv. Energy Mater. 10 (2020) 2002955.
[19] X. Wu, S. Zhao, L. Yin, et al., Chin. Chem. Lett. 34 (2023) 108016.
[20] J. Zhang, Q. Zhang, X. Feng, Adv. Mater. 31 (2019) 1808167.
[21] H. Wang, H. Dai, Chem. Soc. Rev. 42 (2013) 3088–3113.
[22] X. Ren, T. Wu, Y. Sun, et al., Nat. Commun. 12 (2021) 2608.
[23] C.F. Li, J.W. Zhao, L.J. Xie, J.Q. Wu, G.R. Li, Appl. Catal. B: Environ. 291 (2021) 119987.
[24] X. Wang, J. Zhang, P. Wang, et al., Energy Environ. Sci. 16 (2023) 5500–5512.
[25] Y. Liao, Y. Chen, L. Li, et al., Adv. Funct. Mater. 33 (2023) 2303300.
[26] F. He, Q. Zheng, X.X. Yang, et al., Adv. Mater. 35 (2023) 2304022.
[27] F. He, Y.J. Zhao, X.X. Yang, et al., ACS Nano 16 (2022) 9523–9534.
[28] K. Zhu, J. Chen, W. Wang, et al., Adv. Funct. Mater. 30 (2020) 2003556.
[29] F. Chang, P. Su, U. Guharoy, et al., Chin. Chem. Lett. 34 (2023) 107462.
[30] G. Cai, W. Zhang, L. Jiao, S.H. Yu, H.L. Jiang, Chem 2 (2017) 791–802.
[31] F.P. Cheng, X.Y. Peng, L.Z. Hu, et al., Nat. Commun. 13 (2022) 6486.
[32] F.P. Cheng, Z.J. Li, L. Wang, et al., Mater. Horiz. 8 (2021) 556–564.
[33] Z. Jiang, L. Zheng, C. Sheng, et al., J. Colloid Interface Sci. 626 (2022) 848–857.
[34] Y. Liao, S. Deng, Y. Qing, et al., J. Energy Chem. 76 (2023) 566–575.
[35] J. Kang, F. Yang, C. Sheng, et al., Small 18 (2022) 2200950.
[36] C. Yang, Q. Wu, W. Xie, et al., Nature 598 (2021) 590–596.
[37] T. Ouyang, Y.Q. Ye, C.Y. Wu, K. Xiao, Z.Q. Liu, Angew. Chem. Int. Ed. 58 (2019) 4923–4928.
[38] D. Guo, Z. Zeng, Z. Wan, et al., Adv. Funct. Mater. 31 (2021) 2101324.
[39] Y. Kim, D. Kim, J. Lee, L.Y.S. Lee, D.K.P. Ng, Adv. Funct. Mater. 31 (2021) 2103290.
[40] Q. Zhou, S. Hou, Y. Cheng, et al., Appl. Catal. B: Environ. 295 (2021) 120281.
[41] H. Xu, Z.X. Shi, Y.X. Tong, G.R. Li, Adv. Mater. 30 (2018) 1705442.
[42] Q. Guo, Y. Ma, T. Chen, et al., ACS Nano 11 (2017) 12658–12667.
[43] Y. Zhou, G. Chen, Q. Wang, et al., Adv. Funct. Mater. 31 (2021) 2102420.
[44] J. Zhang, M. Zhang, Y. Zeng, et al., Small 15 (2019) 1900307.
[45] Q.Y. Xue, Z.M. Xia, W.Y. Gou, et al., ACS Catal. 13 (2023) 400–406.
[46] J.Y. Li, Y.F. Li, Q.Y. Xue, et al., Chin. J. Struct. Chem. 41 (2022) 2207035–2207039.
[47] Y. Zhang, Y. Wu, L. Wan, et al., Appl. Catal. B: Environ. 311 (2022) 121255.
[48] X. Li, J. Zhou, C. Liu, et al., Appl. Catal. B: Environ. 298 (2021) 120578.
[49] T. Dai, X. Zhang, M. Sun, et al., Adv. Mater. 33 (2021) 2102593.
[50] Z. Wang, P. Wu, X. Zou, et al., Adv. Funct. Mater. 33 (2023) 2214275.
[51] L. Wu, X. Shen, Z. Ji, et al., Adv. Funct. Mater. 33 (2022) 2208170.
[52] T.X. Nguyen, Y.H. Su, C.C. Lin, J.M. Ting, Adv. Funct. Mater. 31 (2021) 2106229.
[53] Y. He, F. Yan, X. Zhang, et al., Adv. Energy Mater. 13 (2023) 2204177.
[54] Y. Deng, Y. Cao, Y. Xia, et al., Adv. Energy Mater. 12 (2022) 2202394.
[55] G. Mu, G. Wang, Q. Huang, et al., Adv. Funct. Mater. 33 (2023) 2211260.
[56] X. Wang, X. Xu, Y. Nie, R. Wang, J. Zou, Adv. Sci. 10 (2023) 2301961.
[57] J. Cai, H. Zhang, L. Zhang, et al., Adv. Mater. 35 (2023) 2303488.
[58] X. Deng, Z. Jiang, Y. Chen, et al., Chin. Chem. Lett. 34 (2023) 107389.
[59] T. Wang, G. Nam, Y. Jin, et al., Adv. Mater. 30 (2018) 1800757.
[60] K. Xiao, Y. Wang, P. Wu, L. Hou, Z.Q. Liu, Angew. Chem. Int. Ed. 62 (2023) e202301408.